Efficient photocatalytic hydrogen production over solid solutions Sr$_{1-x}$Bi$_x$Ti$_{1-x}$Fe$_x$O$_3$ ($0 \leq x \leq 0.5$)

Lingwei Lu [a], Meilin Lv [a], Di Wang [a], Gang Liu [b], Xiaoxiang Xu [a,*]

[a] Shanghai Key Lab of Chemical Assessment and Sustainability, Department of Chemistry, Tongji University, 1239 Siping Road, Shanghai 200092, China
[b] Shenyang National laboratory for Materials Science, Institute of Metal Research, Chinese Academy of Science, 72 Wenhua Road, Shenyang 110016, China

A B S T R A C T

Constituting solid solutions for prototype perovskite compound SrTiO$_3$ offers appealing means to tailor the optical and photocatalytic properties of this wide band gap semiconductor. Here we successfully synthesized a series of Sr$_{1-x}$Bi$_x$Ti$_{1-x}$Fe$_x$O$_3$ ($0 \leq x \leq 0.5$) solid solutions via hydrothermal method. Their crystal structures, surface nature and other physicochemical properties were systematically explored. Our results show that a large portion of BiFeO$_3$ (up to 50%) can be incorporated into the structure SrTiO$_3$ without symmetry degradation from cubic. A number of important factors such as microstructures, light absorbance and surface hydrophilicity are all strongly correlated with Bi/Fe content in the solid solutions. Photocatalytic performance was greatly improved after formation of solid solutions and high activity normally occurs in samples with large surface area, high crystallinity as well as absence of Bi (V) species. The highest activity belongs to sample Sr$_{0.6}$Bi$_{0.4}$Ti$_{0.6}$Fe$_{0.4}$O$_3$ with photocatalytic hydrogen production rate $\sim$50 μmol/h under full range irradiation and $\sim$5 μmol/h under visible light irradiation, corresponding to apparent quantum efficiency $\sim$0.63% and 0.11%, respectively. Theoretical calculation reveals the critical role of Fe in constituting spin-polarized bands inside the intrinsic band gap of SrTiO$_3$, therefore is responsible for band gap reduction and visible light activities. This work highlights the benefits of forming solid solutions in the design and development of efficient photocatalysts.

© 2016 Elsevier B.V. All rights reserved.

1. Introduction

Searching and/or developing alternative clean energy resources have become an increasingly urgent task, not only because our fossil fuel based economy is not sustainable in essence, but also because of various environmental issues associated with fossil fuel usage [1–3]. Photocatalytic water cleavage into hydrogen and oxygen, driven by solar energy, has been considered as a promising means to establish a renewable energy infrastructure as hydrogen is a clean energy vector whilst solar energy is inexhaustible in nature and widely accessible all over the world [4–15]. The scalable application of this technique essentially hinges on the fundamental improvement of photocatalytic materials, which by far, lies in the development of visible light active semiconductors. However, most of semiconductors investigated previously have an intrinsic band gap too large to harvest visible light photons, therefore, suffered from low solar energy conversion efficiency [16,17]. Apart from searching new semiconductors, conventional wide band gap

semiconductors can be modified to be visible light active by introducing foreign atoms into their crystal structure [18–20]. This is mostly evident in SrTiO$_3$, a typical wide band gap semiconductor (band gap $\sim$3.2 eV). For instance, by applying different doping schemes such as simple B site doping (e.g. Cr [21–24], Ni [25], Mn [26,27], Rh [28], etc.), B site co-doping (e.g. Cr/Ta [21], Ni/Nb [25], Rh/Sb [29] etc.) and A/B site co-doping (e.g. La/Cr [30,31], Ag/Nb [32], La/Rh [33], La/Ni [34], etc.), SrTiO$_3$ become visible light active whose photocatalytic properties can be tuned to meet different applications. The allure of SrTiO$_3$ for photocatalytic and/or photoelectrochemical water splitting stems from following facts: (1) it has a comparable band gap to TiO$_2$ but with a conduction band edge alignment ($\sim$−0.5 V vs. NHE) [8,35]; (2) it has an ideal perovskite structure which is extremely tolerant to different cationic and/or anionic replacement[36]; (3) it has a high chemical stability [37,38] and (4) it can be easily synthesized by a wealth of methods and fabricated into membrane or other shapes in accord to different requirements [19,30,39]. Thereby, SrTiO$_3$ is continuously attracting much attention and great efforts have been devoted into modification of its optical and photocatalytic properties. Theoretical calculation have suggested that Cr is one of the most efficient dopants for improving light absorption of SrTiO$_3$ and La is the

* Corresponding author.
  E-mail addresses: xxxu@tongji.edu.cn, xiaoxiangx@gmail.com (X. Xu).

most effective donor to maintain the charge balance and stabilize Cr^{3+} from oxidizing into Cr^{6+} [31]. Later investigation on La/Cr co-doped $SrTiO_3$ confirmed its superior photocatalytic activity in releasing H_2 from water under visible light illumination [19,30,40]. Nevertheless, recent report discloses the negative role of La upon the photocatalytic activity of perovskites by blocking surface catalytic active sites [41] whilst Cr usage always bears environmental risks [42]. Therefore, it is highly desired to develop alternative doping schemes for $SrTiO_3$. In this work, we carried out an investigation on Bi/Fe co-doped $SrTiO_3$ synthesized by hydrothermal method. Bi^{3+}/Fe^{3+} has similar ionic radius with Sr^{2+}/Ti^{4+} so that solid solutions between $BiFeO_3$ and $SrTiO_3$ can be easily formed [43]. The appropriate size, charge and low toxicity of Bi^{3+}/Fe^{3+} doping pair suggest a promising alternative to La^{3+}/Cr^{3+} for $SrTiO_3$ modifications. More importantly, multiferroic compound $BiFeO_3$ has instability issues for water reduction ($BiFeO_3$ reduction potential ~0.3 V vs RHE), although $BiFeO_3$ owns a number of attractive physicochemical properties such as diode effect [44], photovoltaic effect [44–46], pyro-catalytic effect [47] and photocatalytic effect [48,49]. Recent study highlights the benefit of constituting $SrTiO_3$-$BiFeO_3$ solid solutions in enhancing chemical stability of $BiFeO_3$ [50]. It is therefore of great importance to closely investigate the photocatalytic properties of $SrTiO_3$-$BiFeO_3$ solid solutions.

2. Experimental

2.1. Material synthesis

$Sr_{1-x}Bi_xTi_{1-x}Fe_xO_3$ ($0 \leq x \leq 0.5$) solid solutions were prepared via hydrothermal method: appropriate amounts of titanium isopropanol (Aladdin, 95%) were dissolved in anhydrous ethanol (Aladdin) whilst calculated amounts of $Sr(CH_3COO)_2$ (Aladdin, 99%), $Bi(NO_3)_3 \cdot 5H_2O$ (Aladdin, 99%) and $Fe(NO_3)_3 \cdot 9H_2O$ (Aladdin, 99%) were dissolved in deionized water according to stoichiometric ratio. A few drops of concentrated nitric acid were added first to prevent hydrolysis of Bi cations. The two transparent solutions were then slowly mixed under vigorous stirring for 2 h, after which 10 ml 10 M NaOH solution was added dropwisely. The resulting suspension was kept under magnetic stirring for 1 h and was transferred into PTFE-lined autoclaves for hydrothermal reactions. Typical reaction conditions are 200 °C for 48 h. Powders obtained after reaction were washed with deionized water until pH reached 7 and were then dehydrated in an oven at 80 °C for 10 h. $BiFeO_3$ was also synthesized under the same conditions for comparison purpose.

2.2. Methods for analysis

Phase purity and crystal structure were examined by X-ray diffraction (XRD) techniques at a Bruker D8 Focus diffractometer. Incident radiation were Cu $K\alpha_1$ ($\lambda = 1.5406$ Å) and Cu $K\alpha_2$ ($\lambda = 1.5444$ Å). Step size and duration time for data collection were 0.01° and 100 s, respectively. General Structure Analysis System (GSAS) software package was applied to perform Rietveld refinement on the data collected [51]. Microstructures of as-prepared samples were inspected using a field emission scanning electron microscope (Hitachi S4800) and transmission electron microscope (JEOL JEM-2100). Surface conditions and bind energy of constituent elements were analyzed using X-ray photoelectron spectroscopy (Thermo Escalab 250 with a monochromatic Al $K\alpha$ X-ray source). All binding energy were referred to adventitious carbon C 1s peak at 284.7 eV [52]. UV–vis absorption spectra were collected and analyzed on a UV–vis spectrophotometer (JASCO-V750) and JASCO software suite, the reference non-absorbing material is $BaSO_4$ [53]. Atomic compositions of as-prepared samples were analysed by

Inductively Coupled Plasma Techniques (ICP) (Perkin-Elmer PE Optima 2100 DV).

2.3. Photocatalytic hydrogen production

Photocatalytic hydrogen production was carried out in a top-irradiation-type reactor connected to a gas-closed circulation and evacuation system (Perfect Light, Labsolar-IIIAG). In a typical experiment, 100 mg sample powders were ultrasonically dispersed in 100 ml aqueous sodium sulfite solution (0.05 M). The suspension was then sealed in the reactor and subjected to evacuation for air removal. Pt (1 wt%) was applied as a co-catalyst and was loaded onto sample powders by a thermal deposition method: proper amounts of H_2PtCl_6 aqueous solution was impregnated into sample powders and was heated on a hot-plate at 90 °C until dry. The temperature was then raised to 180 °C for 2 h to fully convert H_2PtCl_6 into Pt nanoparticles [9,54]. A 500 W high-pressure mercury lamp (NbeT, Merc-500) was used as a light source. Visible light illumination was generated by filtering the lamp output with a UV cutoff filter ($\lambda \geq 400$ nm). The photon flux of the lamp is calibrated using a quantum meter (Apogee MP-300). The recorded photon flux is ~1543.9 $\mu mol/m^2/s$ for full range irradiation ($\lambda \geq 250$ nm) and ~796.5 $\mu mol/m^2/s$ for visible light irradiation ($\lambda \geq 400$ nm). Water jacket was used to stabilize reactor temperature around 20 °C. The gas component within the reactor was then analyzed using an on-lined gas chromatograph (TECHCOMP, GC7900) with a thermal conductivity detector (5 Å molecular sieve columns and Ar carrier). The apparent quantum efficiency is then calculated using following equation:

$$\text{Apparent quantum efficiency} = 2 \times \text{mol of hydrogen}$$

$$\text{production per hour/mol of photon flux per hour} \times 100\%$$

2.4. Theoretical calculations

Theoretical calculations were performed using the density functional theory (DFT) implemented in the Vienna ab initio simulation package (VASP) [55]. Perdew, Burke and Ernzerhof (PBE) exchange-correlation functional within the generalized gradient approximation (GGA) [56] and the projector augmented-wave pseudopotential were applied [57]. Spin-polarization was also considered during calculation. A $SrTiO_3$ unit cell ($a = b = c = 7.8$ Å, $\alpha = \beta = \gamma = 90°$) with cubic symmetry was built for calculations (total atom number = 40). The solid solution was simulated by replacing 1 Sr atom and 1 Ti atom with 1 Bi atom and 1 Fe atom, giving nominal chemical formula $Sr_{0.875}Bi_{0.125}Ti_{0.875}Fe_{0.125}O_3$. All geometry structures were fully relaxed until the forces on each atom are less than 0.01 eV/Å. Static calculations were performed with a $4 \times 4 \times 4$ Monkhorst-Pack k-point grid [58].

3. Results and discussion

3.1. Phase purity and crystal structure

X-ray powder diffraction (XRD) patterns of as-prepared solid solutions $Sr_{1-x}Bi_xTi_{1-x}Fe_xO_3$ ($0 \leq x \leq 0.5$) and $BiFeO_3$ are illustrated in Fig. 1. Solid solutions all display similar sharp diffraction patterns with pristine $SrTiO_3$ and can be well-indexed using a cubic symmetry, indicating the formation of a single phase. Peak splitting and extra diffraction peaks, such as those seen in pristine $BiFeO_3$ are not observable in all solid solutions, suggesting that cubic framework of $SrTiO_3$ is maintained even with a substantial amounts of Bi/Fe incorporation (up to 50%). Previous investigation fails to reach a cubic single phase compound at $BiFeO_3$ content

Table 1
Space group, unit cell parameters and BET surface area of samples prepared.

Sample	Space group	a/Å	c/Å	V/Å³	BET surface area/m² g⁻¹
$SrTiO_3$	$Pm\bar{3}m$	3.9132(1)	–	59.925(4)	10.2180
$Sr_{0.9}Bi_{0.1}Ti_{0.9}Fe_{0.1}O_3$	$Pm\bar{3}m$	3.9181(2)	–	60.149(5)	13.2211
$Sr_{0.8}Bi_{0.2}Ti_{0.8}Fe_{0.2}O_3$	$Pm\bar{3}m$	3.9201(2)	–	60.243(7)	6.6017
$Sr_{0.7}Bi_{0.3}Ti_{0.7}Fe_{0.3}O_3$	$Pm\bar{3}m$	3.9277(2)	–	60.595(6)	4.4595
$Sr_{0.6}Bi_{0.4}Ti_{0.6}Fe_{0.4}O_3$	$Pm\bar{3}m$	3.9332(2)	–	60.848(8)	2.7584
$Sr_{0.5}Bi_{0.5}Ti_{0.5}Fe_{0.5}O_3$	$Pm\bar{3}m$	3.9438(2)	–	61.343(11)	6.7677
$BiFeO_3$	$R3c$	5.5793(3)	13.8706(9)	373.938(54)	1.3510

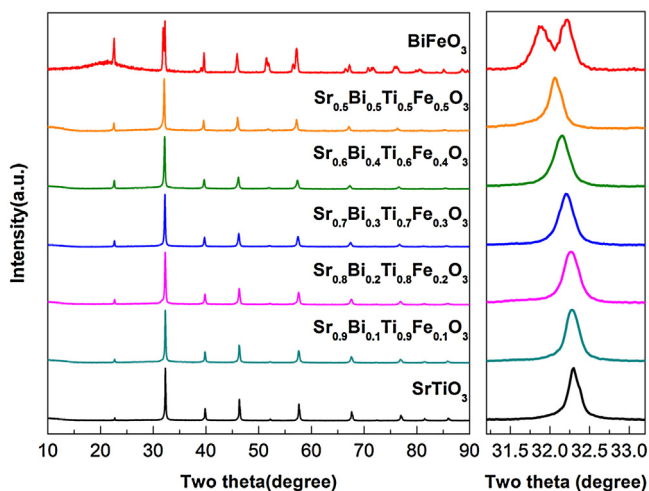**Fig. 1.** X-ray powder diffraction patterns of as-prepared samples. (011) diffraction peak are enlarged for clarity on the right.

Table 2
Atomic compositions of as-prepared samples from ICP analysis.

Sample	Sr (at%)	Bi (at%)	Ti (at%)	Fe (at%)	O (at%)
$SrTiO_3$	9.18	–	11.30	–	79.52
$Sr_{0.9}Bi_{0.1}Ti_{0.9}Fe_{0.1}O_3$	10.22	1.46	12.57	1.23	74.52
$Sr_{0.8}Bi_{0.2}Ti_{0.8}Fe_{0.2}O_3$	10.85	3.16	12.09	2.31	71.58
$Sr_{0.7}Bi_{0.3}Ti_{0.7}Fe_{0.3}O_3$	9.16	4.49	10.21	3.50	72.65
$Sr_{0.6}Bi_{0.4}Ti_{0.6}Fe_{0.4}O_3$	9.16	6.96	10.17	5.57	68.14
$Sr_{0.5}Bi_{0.5}Ti_{0.5}Fe_{0.5}O_3$	7.62	8.56	8.13	6.56	69.13
$BiFeO_3$	–	18.79	–	20.37	60.84

by setting up the constraints that Sr and Bi, Ti and Fe occupy the same crystallographic position, respectively. This again confirms the solid solution formation. In case of pristine $BiFeO_3$, a rhombohedral unit cell (space group $R3c$) is needed for refinement. The structure of $BiFeO_3$ can be viewed as a distorted perovskite lattice originated from sequential rotation of FeO_6 octahedrons along pseudocubic [111] direction and a concomitant off-center of Fe in these octahedrons (ferroelectricity) [59]. Such a large structural distortion in pristine $BiFeO_3$ indirectly manifests the superior tolerance of $SrTiO_3$ towards cation replacement without degradation from cubic symmetry. The refined unit cell parameters are plotted in Fig. 3 and tabulated in Table 1. As can be seen in Fig. 3, unit cell of solid solutions $Sr_{1-x}Bi_xTi_{1-x}Fe_xO_3$ ($0 \leq x \leq 0.5$) gradually expands upon Bi/Fe incorporation, which strictly obeys Vegard's law. The atomic compositions of solid solutions were then analyzed using ICP techniques, which are tabulated in Table 2. The atom ratios are consistent with nominal chemical formulas thereby confirms again the formation of solid solutions between $SrTiO_3$ and $BiFeO_3$.
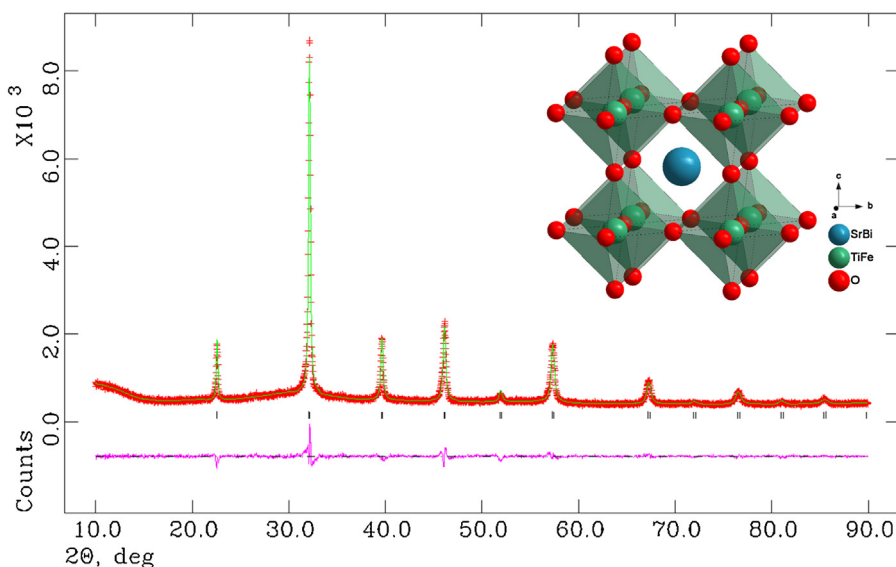
higher than 20% ($x \geq 0.2$) and is likely due to a high temperature synthetic method used that may experience severe Bi losses [43]. The solid solution formation is better illustrated by focusing on the strongest (011) diffraction peak which undergoes a clear shift to small angles along with Bi/Fe incorporation (Fig. 1 right). We then performed Rietveld refinement on the diffraction data. Typical refinement results of $Sr_{0.8}Bi_{0.2}Ti_{0.8}Fe_{0.2}O_3$ are displayed in Fig. 2 using a primitive cubic unit cell (space group $Pm\bar{3}m$). Reasonable goodness-of-fit parameters (R_p, R_{wp} and χ^2) were only achieved

Fig. 2. Observed and calculated X-ray powder diffraction patterns of $Sr_{0.8}Bi_{0.2}Ti_{0.8}Fe_{0.2}O_3$. The refinement converged with good R-factors (R_p = 4.84%, R_{wp} = 3.69%, χ^2 = 1.325), the refined crystal structure is schematically shown in the images inserted as a visualization.
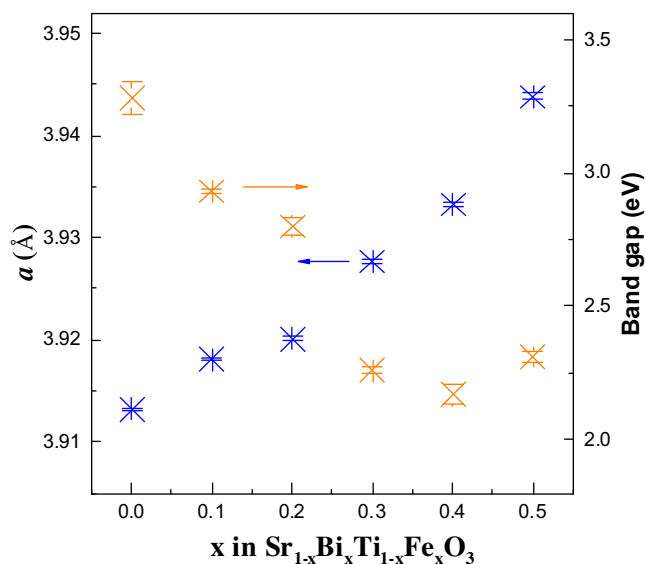
Fig. 3. Refined unit cell parameters and band gap values calculated from UV–vis spectra of freshly prepared samples.

3.2. Microstructures

Microstructures of semiconductors often exert strong impact on their photocatalytic performance [60,61]. We then carried out an examination on the microstructures of as-prepared samples. Fig. 4 shows the SEM images of freshly prepared samples and a photograph of their powder appearance. It can be seen from SEM images that microstructures of individual samples are substantially influenced by $BiFeO_3$ content in the solid solution. Distinctive morphologies that contain either spherical or cubic particles can be generated by varying Bi/Fe content in $Sr_{1-x}Bi_xTi_{1-x}Fe_xO_3$ ($0 \leq x \leq 0.5$). For samples with relatively low or high Bi/Fe content, particles are mainly spherical and are essentially made up of agglomerations of nano-sized grains. At intermediate Bi/Fe content ($Sr_{0.6}Bi_{0.4}Ti_{0.6}Fe_{0.4}O_3$), however, cubic particles exposing (100) crystal facets dominate. Similar observations have also seen in other doping systems involving Bi and are attributed to self-assembly of nano-sized grains by sharing identical crystallographic orientations. The underlying mechanism for triggering such self-assembling process is not clear, probably correlated with different surface free energy of nano-sized grains at different Bi/Fe content [19]. Pristine $BiFeO_3$, on the other hand, exhibits large grains with clear crystal facet and sharp grain edges under SEM conditions (Fig. 4g).

Microstructures of individual particles were further analyzed under transmission electron microscopy conditions (TEM). Fig. 5 shows the typical TEM images of single particle for $Sr_{0.9}Bi_{0.1}Ti_{0.9}Fe_{0.1}O_3$ and $Sr_{0.6}Bi_{0.4}Ti_{0.6}Fe_{0.4}O_3$. The polycrystalline nature of spherical particles in $Sr_{0.9}Bi_{0.1}Ti_{0.9}Fe_{0.1}O_3$ is confirmed by selected area electron diffraction (SAED) patterns containing a series of diffraction rings. High resolution TEM image
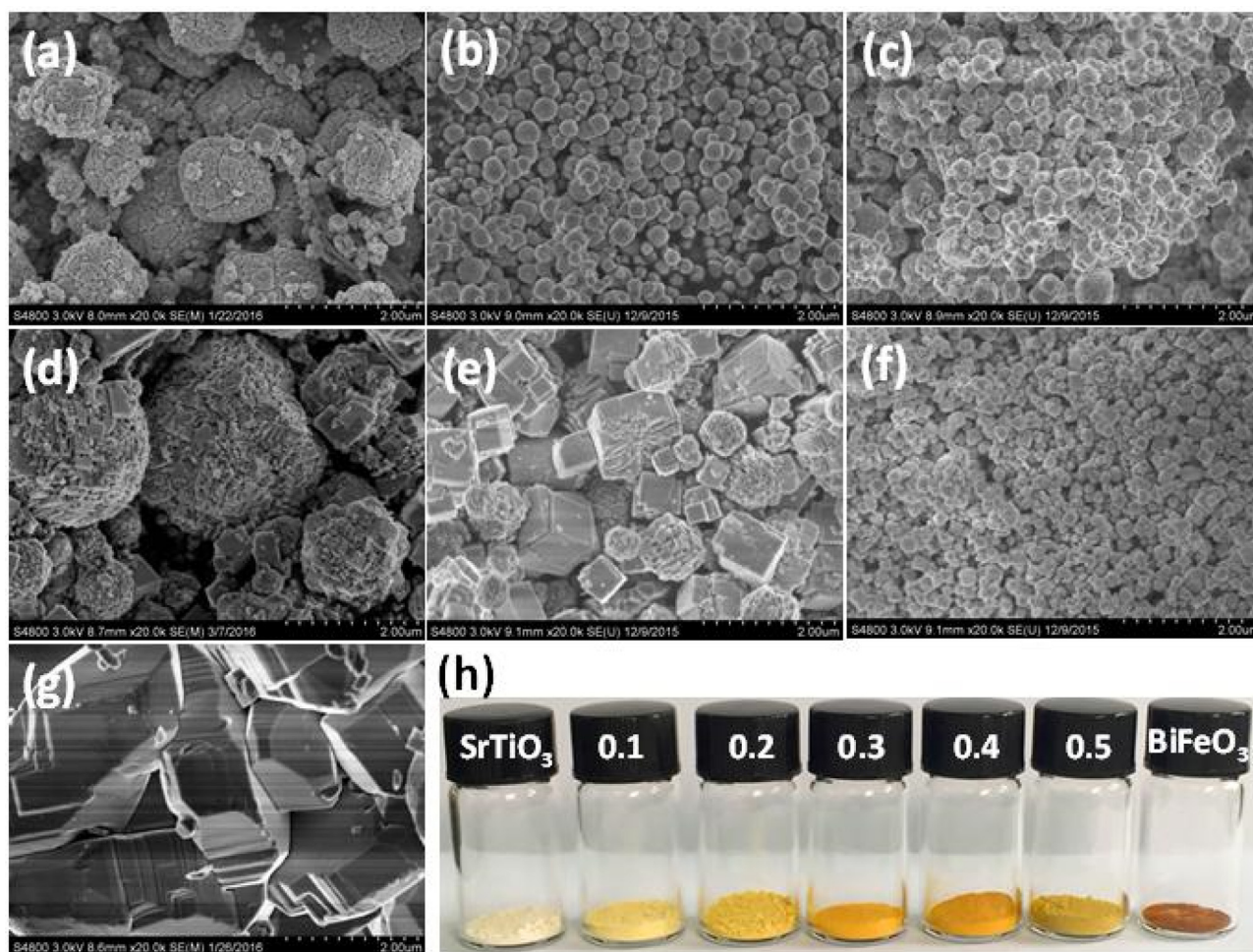

Fig. 4. Field emission scanning electron microscopy images of $Sr_{1-x}Bi_xTi_{1-x}Fe_xO_3$ (a) $SrTiO_3$ (x = 0), (b) x = 0.1, (c) x = 0.2, (d) x = 0.3, (e) x = 0.4, (f) x = 0.5, (g) $BiFeO_3$ (x = 1) and (h) a photograph of as-prepared sample powders.
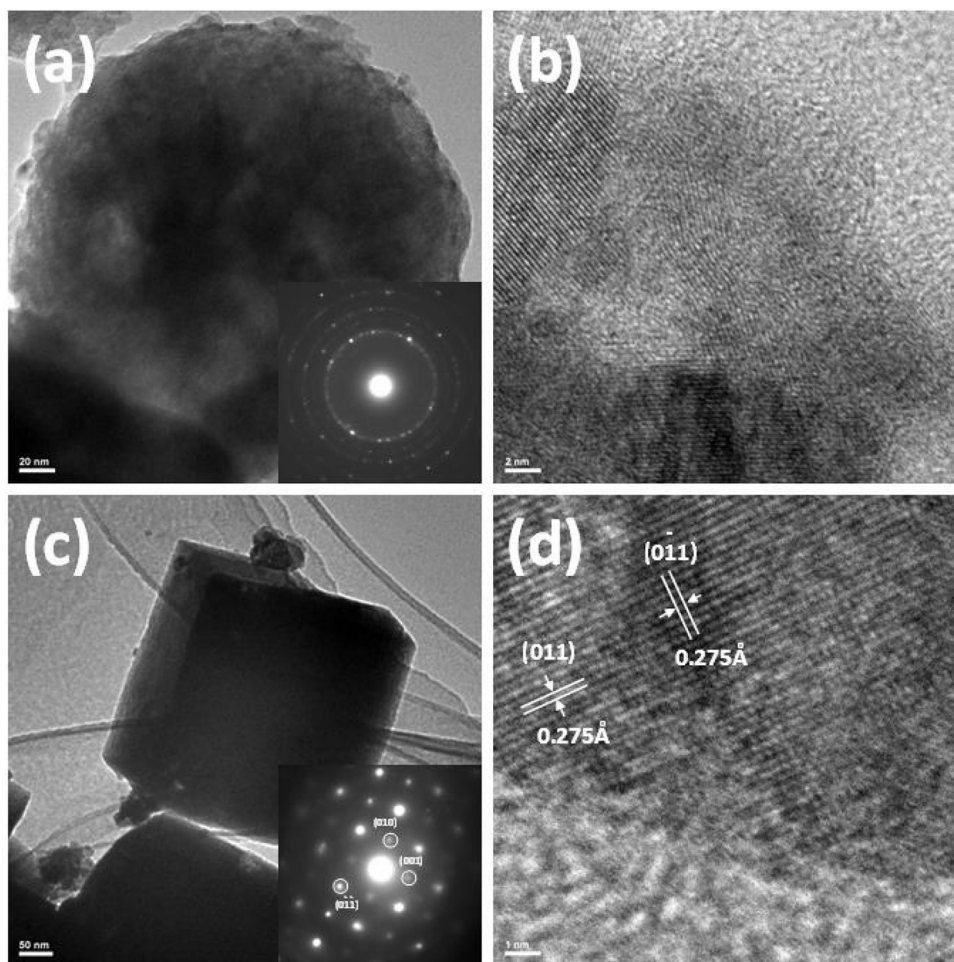
Fig. 5. Transmission electron microscopy (TEM) and high-resolution TEM images of selected particles of sample $Sr_{0.9}Bi_{0.1}Ti_{0.9}Fe_{0.1}O_3$ (a) and (b); sample $Sr_{0.6}Bi_{0.4}Ti_{0.6}Fe_{0.4}O_3$ (c) and (d), images of selected area electron diffraction (SAED) patterns of the whole particles are inserted.

reveals its fine structure to be agglomeration of randomly oriented nano-crystallines (Fig. 5b). On the contrary, particles of $Sr_{0.6}Bi_{0.4}Ti_{0.6}Fe_{0.4}O_3$ are in fact cubic single crystalline, as can be seen from the characteristic diffraction spots in SAED patterns taken along 100 zone axis as well as regular lattice fringes under high resolution TEM conditions (Fig. 5d).

The color of freshly prepared samples is white for pristine $SrTiO_3$, reddish brown for pristine $BiFeO_3$ and yellow/orange for solid solutions $Sr_{1-x}Bi_xTi_{1-x}Fe_xO_3$ ($0 < x \leq 0.5$) (Fig. 4h). The strong color after Bi/Fe incorporation implies substantial visible light absorptions. This is confirmed from their UV–vis absorption spectra (Fig. 6). For pristine $SrTiO_3$, the spectrum is characterized by a sharp absorption edge below 400 nm, indicative of its wide band gap nature. However, the absorption edge is considerably red-shifted into visible light region upon Bi/Fe incorporation and is responsible for their colored appearance. Considering the fact that ligand to metal charge transfer (LMCT) for FeO_6 octahedrons normally take place at UV region (275 nm) and Fe^{3+} has a d^5 electronic configuration which is spin, symmetry and parity forbidden for internal d-d transitions under weak crystal field [62]. Such intense absorption in the visible light region (400 nm to 600 nm) can be attributed to metal to metal charge transfer (MMCT) either from $Fe^{3+} \rightarrow Ti^{4+}$ ($Fe^{3+} + Ti^{4+} \rightarrow Fe^{4+} + Ti^{3+}$) or between different Fe^{3+} species ($2Fe^{3+} \rightarrow Fe^{2+} + Fe^{4+}$) [20]. The enhanced absorbance in this region for samples with high Bi/Fe content can be explained by increased Fe incorporation that allows more MMCT. However, such absorption is slightly weakened at high Bi/Fe content

($Sr_{0.5}Bi_{0.5}Ti_{0.5}Fe_{0.5}O_3$) and likely due to unit cell expansion effect that increases metal to metal distances and makes MMCT more difficult. Thereby, band gaps of solid solutions approach a minimum point at x = 0.4 and exhibit a parabolic shape if plotted against Bi/Fe content (Fig. 3). On the other hand, the absorption tail above 600 nm typically belongs to weak d-d transitions of Fe^{3+} in the octahedral crystal field ($^6A_{1g} \rightarrow {}^4A_{1g}$, ^4E_g, $^4T_{1g}$) and normally does not contribute to photocatalytic reactions. Nevertheless, these typical absorptions become much stronger in case of pristine $BiFeO_3$ and can be ascribed to off-centering of Fe^{3+} in FeO_6 octahedrons that breaks centrosymmetry and releases somewhat forbidden rules.

The surface nature of freshly prepared sample was then analyzed by using X-ray photoelectron spectroscopy (XPS). Binding energy of core-level electrons from constituent elements Bi, Fe and O for solid solutions is illustrated in Fig. 7. All signals were referenced to C 1s peak at 284.7 eV, arising from adventitious carbon. Overlapping peaks were unfolded by applying different Gaussian functions. The Bi 4f level all contains two strong peaks around 159 eV and 164 eV, corresponding to Bi $4f_{7/2}$ and Bi $4f_{5/2}$ states of Bi (III). However, additional shoulders at higher energy are occasionally seen (x = 0.1, 0.3 and 0.5), indicating the presence of Bi (V) species [63]. Similar observation was also found in Bi/Cr doped $SrTiO_3$ synthesized at similar conditions [19]. The underlying causes for Bi (III) to be oxidized to Bi (V) in certain samples are not clear, however, this phenomenon is found to be critical in determining photocatalytic performance as Bi (V) species are prone to trap and consume photo-generated electrons [19]. The Fe
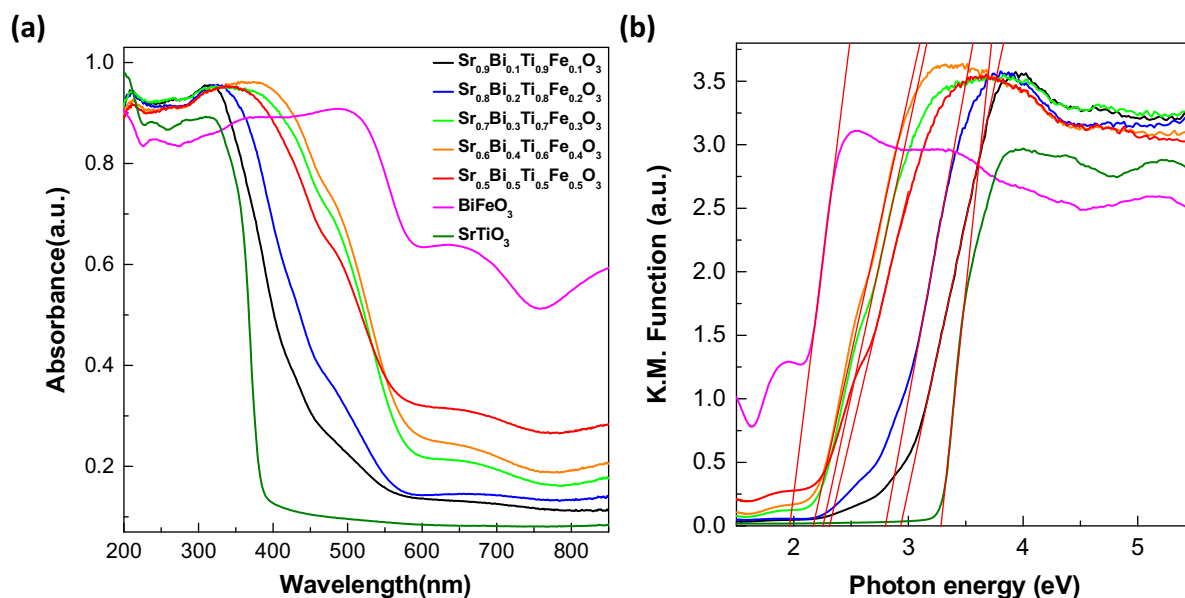
Fig. 6. (a) UV–visible light absorption spectra (converted from diffuse reflectance spectra) of freshly prepared samples and (b) Kubelka-Munk transformation of diffuse reflectance data.
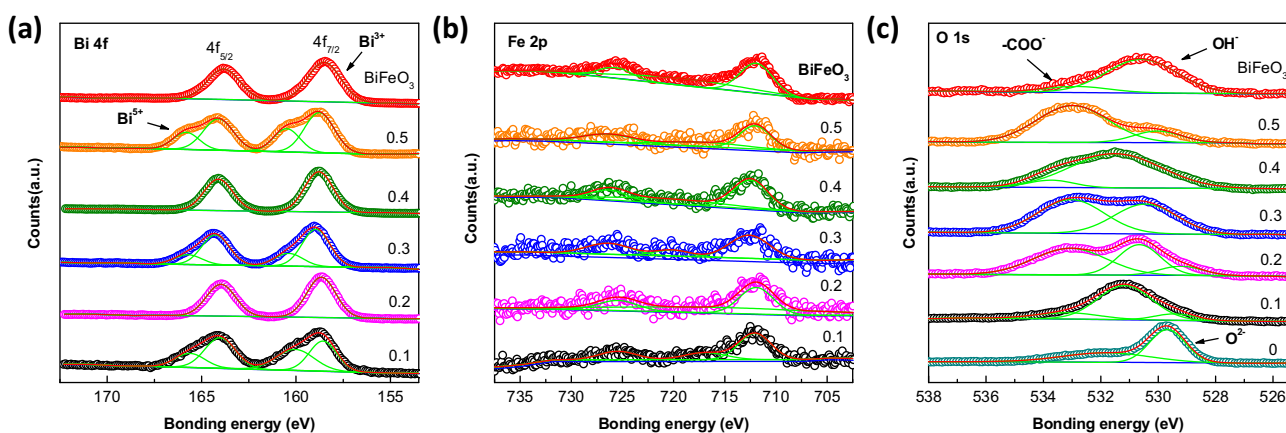

Fig. 7. XPS spectra of freshly prepared samples: (a) Bi 4f peaks, (b) Fe 2p peaks and (c) O 1s peaks.

2p level generally includes two small peaks at 711 eV and 725 eV, corresponding to Fe $2p_{3/2}$ and Fe $2p_{1/2}$ states of Fe^{3+} species [49]. The O 1s level, however, normally contains several broad peaks centered at around 529 eV, 530 eV and 532 eV, assignable to lattice oxygen, OH^- species and carboxylic groups. Introducing Bi/Fe into $SrTiO_3$ seems to have a positive effect in improving the surface hydrophilicity as more OH^- species are found in solid solutions compared with pristine $SrTiO_3$. This effect is more clearly seen in sample $Sr_{0.6}Bi_{0.4}Ti_{0.6}Fe_{0.4}O_3$ where lattice oxygen cannot be detected, presumably due to fully coverage of perovskite surface with OH^- species.

The photocatalytic properties of as-prepared samples were then evaluated by monitoring the hydrogen evolution from aqueous solution under light irradiation. Pt (1 wt%) was loaded as a cocatalyst and sodium sulfite (0.05 M) was used as a sacrificial agent to promote the reactions. Control experiment in the dark was firstly carried out in order to check any spontaneous hydrogen production reactions. No hydrogen was detected for 5 h therefore precluding any reactions that lead to hydrogen evolution spontaneously. Steady hydrogen evolution was detected immediately upon light irradiation and typical temporal hydrogen evolution is illustrated in Fig. 8a. Under full range irradiation ($\lambda \geq 250$ nm), all solid solution samples exhibit improved activity over pristine $SrTiO_3$ and $BiFeO_3$, highlighting the benefit of constituting $SrTiO_3$-$BiFeO_3$ solid solutions. The only exception is $Sr_{0.7}Bi_{0.3}Ti_{0.7}Fe_{0.3}O_3$, presumably due to the presence of a large portion of Bi (V) species at the surface and a small surface area. It is interesting to see that pristine $BiFeO_3$ exhibit the poorest activity albeit it shows the strongest light absorption. The highest activity was found for $Sr_{0.6}Bi_{0.4}Ti_{0.6}Fe_{0.4}O_3$ with an average hydrogen production rate ~50 μmol/h, corresponding to apparent quantum efficiency ~0.63%. This value is twice as much as pristine $SrTiO_3$ and nearly five times higher than pristine $BiFeO_3$. Considering its smallest surface area among all solid solutions (Table 1), such a high activity is superior and is probably a combined result of several factors such as a strong light absorption (small band gap), a high crystallinity (cubic particles) as well as free of detrimental Bi (V) species. More importantly, hydrogen production under visible light irradiation ($\lambda \geq 400$ nm) was only observed in solid solution samples. Fig. 8b illustrates the average hydrogen production rate under both full range and visible light irradiation. It can be summarized from Fig. 8b that photocatalytic activity was governed by a number of parameters including surface area, band gap, crystallinity and presence or absence of Bi (V) species. The highest hydrogen production rate under visible light irradiation
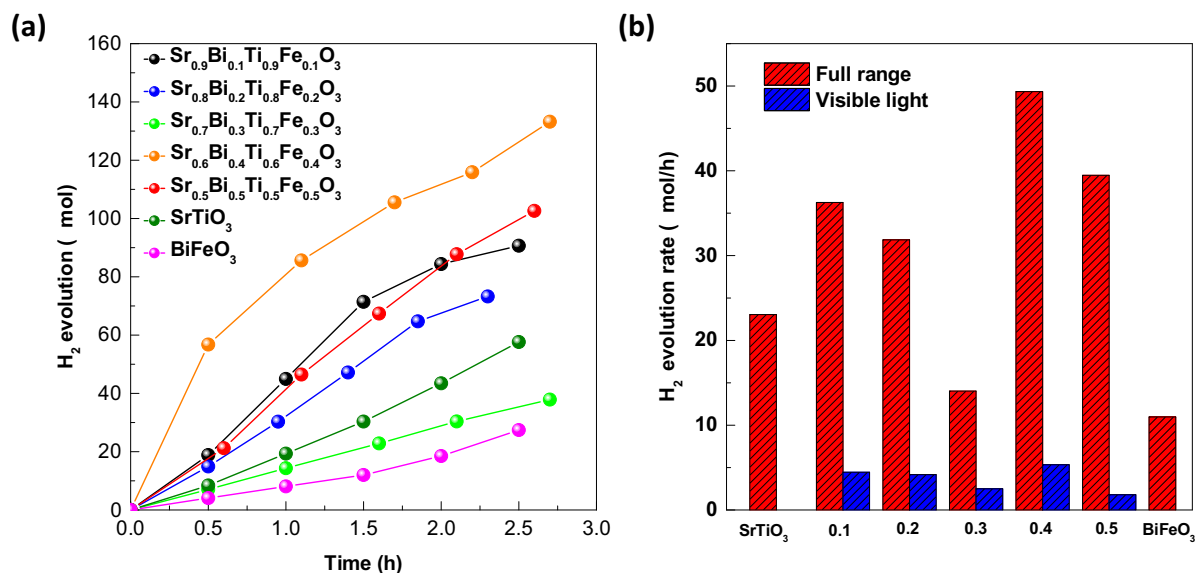
Fig. 8. (a) Photocatalytic hydrogen production of samples under full range irradiation ($\lambda \geq 250$ nm) in sodium sulfite aqueous solution (0.05 M), (b) average photocatalytic hydrogen production rate under full range irradiation ($\lambda \geq 250$ nm) and visible light irradiation ($\lambda \geq 400$ nm).
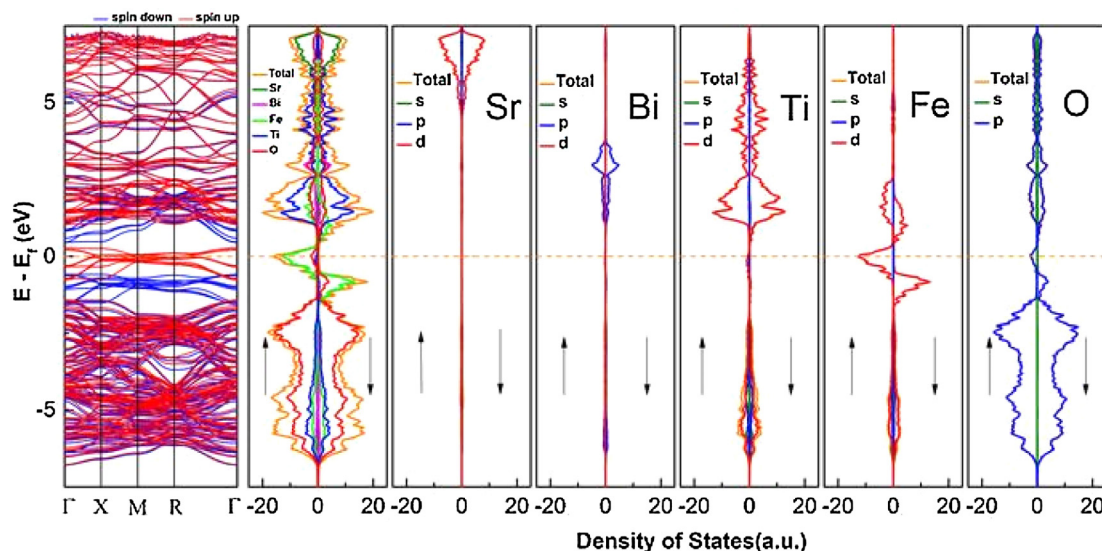

Fig. 9. Calculated band structures, total density of states (DOS) and partial density of states (PDOS) of constituent elements.

also belongs to $Sr_{0.6}Bi_{0.4}Ti_{0.6}Fe_{0.4}O_3$ (~5 μmol/h), corresponding to apparent quantum efficiency ~0.11%. This value was found to be better than or at least comparable to other doped $SrTiO_3$ photocatalysts such as Sb/Rh co-doped $SrTiO_3$ [29], Ta/Ni co-doped $SrTiO_3$ [25], Bi/Cr co-doped $SrTiO_3$ [19], Cr doped $SrTiO_3$ [64] and Ta/Cr co-doped $SrTiO_3$ [21].

For better understanding the optical and photocatalytic properties of $SrTiO_3$-$BiFeO_3$ solid solutions, we carried out a theoretical calculation on electronic structures using density functional theory (DFT). Solid solutions were simulated based on a $SrTiO_3$ unit cell by partially substituting Sr and Ti with Bi and Fe atoms, respectively. The band structure and density of states (DOS) near Fermi levels are illustrated in Fig. 9. Apart from the typical conduction band (CB) dominated by Ti 3d orbitals and valence band (VB) made of O 2p orbitals [65,66], two sets of spin-polarized bands were formed inside the band gap. These newly formed bands are mainly comprised of Fe 3d orbitals and are responsible for the band gap reduction and visible light absorption. Although Fermi level (set

at zero energy) now dwell inside these bands, the compound is essentially a semiconductor as Fe 3d electrons are highly localized [67]. It is interesting to see from DOS that CB also has contributions from Fe, indicating orbital hybridization between Ti 3d and Fe 3d orbitals. Therefore, the visible light absorption and photocatalytic activity can be understood as electron excitations from occupied Fe 3d orbitals to either empty Ti 3d orbitals or Fe 3d orbitals, i.e. $Fe^{3+} + Ti^{4+} \rightarrow Fe^{4+} + Ti^{3+}$ or $2Fe^{3+} \rightarrow Fe^{2+} + Fe^{4+}$.

4. Conclusions

We have successfully synthesized a series of $Sr_{1-x}Bi_xTi_{1-x}Fe_xO_3$ ($0 \leq x \leq 0.5$) solid solutions via hydrothermal method. Their crystal structure, microstructures, optical properties, surface conditions as well as photocatalytic activity were systematically investigated. Our results show that cubic symmetry of perovskite was maintained up to 50% Bi/Fe incorporations. Their microstructures contain either spherical or cubic particles and are controlled by

Bi/Fe content in the structure. TEM analysis revealed that the spherical particles are polycrystalline with agglomerations of randomly oriented nano-sized grains while cubic ones are essentially single crystalline. Constituting solid solutions between $SrTiO_3$-$BiFeO_3$ is an efficient way to modify the band gap of $SrTiO_3$ and extend light absorption into visible light region. The surface hydrophilicity of $SrTiO_3$ was also improved upon Bi/Fe incorporation although detrimental Bi (V) species were occasionally found. The solid solutions generally demonstrated enhanced photocatalytic hydrogen production under both full range ($\lambda \geq 250$ nm) and visible light irradiation ($\lambda \geq 400$ nm). High activity normally occurs in samples with high surface area, high crystallinity and free of Bi (V) species. The highest hydrogen production rate observed is $\sim$50 μmol/h under full range irradiation and $\sim$5 μmol/h under visible light irradiation, corresponding to apparent quantum efficiency $\sim$0.63% and 0.11%, respectively. DFT calculation revealed the critical role of Fe in constituting additional spin-polarized bands inside the intrinsic band gap of $SrTiO_3$. These spin-polarized bands therefore are responsible for the band gap reduction and visible light photocatalytic activity.

Acknowledgements

References

[1] N.S. Lewis, D.G. Nocera, Proc. Natl. Acad. Sci. U. S. A. 103 (2006) 15729–15735.
[2] Annual Energy Outlook 2014, U. S. Energy Information Administration, 2014.
[3] B. Dudley, BP Stat. Rev. World Energy (2014) 2014.
[4] Z.G. Zou, J.H. Ye, K. Sayama, H. Arakawa, Nature 414 (2001) 625–627.
[5] K. Maeda, K. Teramura, D.L. Lu, T. Takata, N. Saito, Y. Inoue, K. Domen, Nature 440 (2006), 295–295.
[6] X.C. Wang, K. Maeda, A. Thomas, K. Takanabe, G. Xin, J.M. Carlsson, K. Domen, M. Antonietti, Nat. Mater. 8 (2009) 76–80.
[7] X.X. Xu, C. Randorn, P. Efstathiou, J.T.S. Irvine, Nat. Mater. 11 (2012) 595–598.
[8] X.X. Xu, C. Liu, C. Randorn, J.T.S. Irvine, Int. J. Hydrogen Energy 36 (2011) 13501–13507.
[9] X.X. Xu, G. Liu, A.K. Azad, Int. J. Hydrogen Energy 40 (2015) 3672–3678.
[10] X.X. Xu, Y.H. Xie, S. Ni, A.K. Azad, T.C. Cao, J. Solid State Chem. 230 (2015) 95–101.
[11] Y.H. Xie, F.F. Wu, X.Q. Sun, H.M. Chen, M.L. Lv, S. Ni, G. Liu, X.X. Xu, Sci. Rep. 5 (2016) 19060.
[12] F.F. Wu, M.L. Lv, X.Q. Sun, Y.H. Xie, H.M. Chen, S. Ni, G. Liu, X.X. Xu, ChemCatChem 8 (2016) 615–623.
[13] M.L. Lv, S. Ni, Z. Wang, T.C. Cao, X.X. Xu, Int. J. Hydrogen Energy 41 (2016) 1550–1558.
[14] H.M. Chen, Y.H. Xie, X.Q. Sun, M.L. Lv, F.F. Wu, L. Zhang, L. Li, X.X. Xu, Dalton Trans. 44 (2015) 13030–13039.
[15] Y.H. Xie, Y.W. Wang, Z.F. Chen, X.X. Xu, ChemSusChem 9 (2016) 1403–1412.
[16] A. Kudo, Y. Miseki, Chem. Soc. Rev. 38 (2009) 253–278.
[17] X.B. Chen, S.H. Shen, L.J. Guo, S.S. Mao, Chem. Rev. 110 (2010) 6503–6570.
[18] X.Q. Sun, Y.H. Xie, F.F. Wu, H.M. Chen, M.L. Lv, S. Ni, G. Liu, X.X. Xu, Inorg. Chem. 54 (2015) 7445–7453.
[19] M.L. Lv, Y.H. Xie, Y.W. Wang, X.Q. Sun, F.F. Wu, H.M. Chen, S.W. Wang, C. Shen, Z.F. Chen, S. Ni, G. Liu, X.X. Xu, Phys. Chem. Chem. Phys. 17 (2015) 26320–26329.
[20] X.X. Xu, A.K. Azad, J.T.S. Irvine, Catal. Today 199 (2013) 22–26.
[21] T. Ishii, H. Kato, A. Kudo, J. Photoch. Photobio. A 163 (2004) 181–186.
[22] U. Sulaeman, S. Yin, T. Sato, Appl. Catal. B-Environ. 105 (2011) 206–210.
[23] H.H. Li, S. Yin, Y.H. Wang, T. Sekino, S.W. Lee, T. Sato, J. Catal. 297 (2013) 65–69.
[24] D.F. Wang, J.H. Ye, T. Kako, T. Kimura, J. Phys. Chem. B 110 (2006) 15824–15830.
[25] R. Niishiro, H. Kato, A. Kudo, Phys. Chem. Chem. Phys. 7 (2005) 2241–2245.
[26] X. Zhou, J.Y. Shi, C. Li, J. Phys. Chem. C 115 (2011) 8305–8311.
[27] G.L. Wu, P. Li, D.B. Xu, B.F. Luo, Y.Z. Hong, W.D. Shi, C.B. Liu, Appl. Surf. Sci. 333 (2015) 39–47.
[28] R. Konta, T. Ishii, H. Kato, A. Kudo, J. Phys. Chem. B 108 (2004) 8992–8995.
[29] R. Asai, H. Nemoto, Q. Jia, K. Saito, A. Iwase, A. Kudo, Chem. Commun. 50 (2014) 2543–2546.
[30] S.X. Ouyang, H. Tong, N. Umezawa, J.Y. Cao, P. Li, Y.P. Bi, Y.J. Zhang, J.H. Ye, J. Am. Chem. Soc. 134 (2012) 1974–1977.
[31] P. Reunchan, S.X. Ouyang, N. Umezawa, H. Xu, Y.J. Zhang, J.H. Ye, J. Mater. Chem. A 1 (2013) 4221–4227.
[32] D.F. Wang, T. Kako, J.H. Ye, J. Am. Chem. Soc. 130 (2008) 2724–2725.
[33] Q. Wang, T. Hisatomi, S.S.K. Ma, Y.B. Li, K. Domen, Chem. Mater. 26 (2014) 4144–4150.
[34] A.Z. Jia, X.Q. Liang, Z.Q. Su, T. Zhu, S.X. Liu, J. Hazard. Mater. 178 (2010) 233–242.
[35] M.S. Wrighton, A.B. Ellis, P.T. Wolczanski, D.L. Morse, H.B. Abrahamson, D.S. Ginley, J. Am. Chem. Soc. 98 (1976) 2774–2779.
[36] R.H. Mitchell, Perovskites: Modern and Ancient, Almaz Press Inc., Ontario, Canada, 2002.
[37] F.T. Wagner, G.A. Somorjai, Nature 285 (1980) 559–560.
[38] D.E. Scaife, Sol. Energy 25 (1980) 41–54.
[39] D.S. Bae, E.J. Kim, S.W. Park, K.S. Han, J. Mater. Sci. 41 (2006) 6162–6164.
[40] X.X. Xu, M.L. Lv, X.Q. Sun, G. Liu, J. Mater. Sci. 51 (2016) 6464–6473.
[41] S.P. Phivilay, A.A. Puretzky, K. Domen, I.E. Wachs, ACS Catal. 3 (2013) 2920–2929.
[42] A.K. Shanker, C. Cervantes, H. Loza-Tavera, S. Avudainayagam, Environ. Int. 31 (2005) 739–753.
[43] D.J. Goossens, C.J. Weekes, M. Avdeev, W.D. Hutchison, J. Solid State Chem. 207 (2013) 111–116.
[44] T. Choi, S. Lee, Y.J. Choi, V. Kiryukhin, S.W. Cheong, Science 324 (2009) 63–66.
[45] S.Y. Yang, J. Seidel, S.J. Byrnes, P. Shafer, C.H. Yang, M.D. Rossell, P. Yu, Y.H. Chu, J.F. Scott, J.W. Ager III, L.W. Martin, R. Ramesh, Nat. Nanotechnol. 5 (2010) 143–147.
[46] A. Bhatnagar, A.R. Chaudhuri, Y.H. Kim, D. Hesse, M. Alexe, Nat. Commun. 4 (2013) 2835.
[47] J. Wu, W. Mao, Z. Wu, X. Xu, H. You, A. Xue, Y. Jia, Nanoscale (2016).
[48] U.A. Joshi, J.S. Jang, P.H. Borse, J.S. Lee, Appl. Phys. Lett. 92 (2008), 242106-242101-242103.
[49] Y. Hou, M. Miao, Y. Zhang, J. Zhu, H. Li, Chem. Commun. 47 (2011) 2089–2091.
[50] S. Cho, J.W. Jang, W. Zhang, A. Suwardi, H. Wang, D. Wang, J.L. MacManus-Driscoll, Chem. Mater. 27 (2015) 6635–6641.
[51] A.C. Larson, R.B. Von Dreele, Los Alamos National Laboratory Report No. LA-UR-86-748, 1994.
[52] P. Van der Heide, X-ray Photoelectron Spectroscopy – An Introduction to Principles and Practices, John Wiley & Sons, Inc, Hoboken, New Jersey, 2012.
[53] G. Kortum, W. Braun, G. Herzog, Angew. Chem. Int. Ed. 2 (1963) 333–341.
[54] X.X. Xu, G. Liu, C. Randorn, J.T.S. Irvine, Int. J. Hydrogen Energy 36 (2011) 13501–13507.
[55] G. Kresse, J. Furthmuller, Phys. Rev. B 54 (1996) 11169–11186.
[56] J.P. Perdew, K. Burke, M. Ernzerhof, Phys. Rev. Lett. 77 (1996) 3865–3868.
[57] G. Kresse, D. Joubert, Phys. Rev. B 59 (1999) 1758–1775.
[58] H.J. Monkhorst, J.D. Pack, Phys. Rev. B 13 (1976) 5188–5192.
[59] J. Seidel, L.W. Martin, Q. He, Q. Zhan, Y.H. Chu, A. Rother, M.E. Hawkridge, P. Maksymovych, P. Yu, M. Gajek, N. Balke, S.V. Kalinin, S. Gemming, F. Wang, G. Catalan, J.F. Scott, N.A. Spaldin, J. Orenstein, R. Ramesh, Nat. Mater. 8 (2009) 229–234.
[60] H.G. Yang, C.H. Sun, S.Z. Qiao, J. Zou, G. Liu, S.C. Smith, H.M. Cheng, G.Q. Lu, Nature 453 (2008), 638–U634.
[61] H.M. Chen, K.H. Xie, X.Q. Sun, M.L. Lv, F.F. Wu, L. Zhang, L. Li, X.X. Xu, Dalton Trans. (2015).
[62] L.G.J. Dehaart, G. Blasse, Solid State Ionics 16 (1985) 137–139.
[63] D.J. Wang, L. Guo, Y.Z. Zhen, L.L. Yue, G.L. Xue, F. Fu, J. Mater, Chem. A 2 (2014) 11716–11727.
[64] J.W. Liu, G. Chen, Z.H. Li, Z.G. Zhang, J. Solid State Chem. 179 (2006) 3704–3708.
[65] B. Modak, S.K. Ghosh, J. Phys. Chem. C 119 (2015) 23503–23514.
[66] W. Chen, H. Liu, X.Y. Li, S. Liu, L. Gao, L.Q. Mao, Z.Y. Fan, W.F. Shangguan, W.J. Fang, Y.S. Liu, Appl. Catal. B-Environ. 192 (2016) 145–151.
[67] P.A. Cox, Transition Metal Oxides: An Introduction to Their Electronic Structure and Properties, Oxford University Press, 1992.